

## Research Article

# Brazeability, Microstructure, and Joint Characteristics of $\text{ZrO}_2/\text{Ti-6Al-4V}$ Brazed by Ag-Cu-Ti Filler Reinforced with Cerium Oxide Nanoparticles

Ashutosh Sharma  and Byungmin Ahn 

Department of Materials Science and Engineering and Department of Energy Systems Research, Ajou University, Suwon 16499, Republic of Korea

Correspondence should be addressed to Byungmin Ahn; [byungmin@ajou.ac.kr](mailto:byungmin@ajou.ac.kr)

Received 30 July 2019; Revised 11 October 2019; Accepted 5 November 2019; Published 12 December 2019

Guest Editor: Rezwanul Haque

Copyright © 2019 Ashutosh Sharma and Byungmin Ahn. This is an open access article distributed under the Creative Commons Attribution License, which permits unrestricted use, distribution, and reproduction in any medium, provided the original work is properly cited.

In this work, we have attempted to develop the Ag-Cu-Ti filler for bonding  $\text{ZrO}_2$  to Ti-6Al-4V. The  $\text{CeO}_2$  nanoparticles were reinforced in the eutectic Ag-Cu-Ti filler via mechanical mixing and melting route. Furthermore, the brazeability, microstructure, and mechanical behavior, as well as brazing performance of the  $\text{ZrO}_2/\text{Ti-6Al-4V}$  joints, were assessed. The wettability of the Ag-Cu-Ti matrix was increased from 89 to 98% on Ti-6Al-4V and from 83 to 89% on the  $\text{ZrO}_2$  substrate after the addition of 0.05%  $\text{CeO}_2$ . Also, there was a depression in the melting point of the composite fillers up to 3°C. The microstructure consists of Cu- and Ag-rich phases and Cu-Ti intermetallic compounds (IMCs). The joint shear strength was improved with the addition of  $\text{CeO}_2$  up to 0.05 wt.% in the matrix. It was inferred that, for an excellent brazing performance of the  $\text{ZrO}_2/\text{Ti-6Al-4V}$  joint, the optimum amount of  $\text{CeO}_2$  should be 0.05 wt.% in the Ag-Cu-Ti matrix.

## 1. Introduction

Bonding of ceramic materials to metals is a recent hot topic in various engineering applications, including heat exchangers, connectors, capacitors, thermoelectrics, solar cells, and complex structural joints [1, 2]. It is always a practical challenge to bond these ceramic materials directly due to a wide difference in physicochemical and mechanical properties of ceramics and metals that imposes a great challenge in microjoining operations [2]. For this purpose, various popular brazing fillers are already developed where the most popular ones are eutectic Ag-Cu or Ag-Cu-Ti alloys as reported in the past [3, 4]. However, with regard to complex geometry, the thickness of IMCs, and cost, each filler is unique and has limitations of its own [5]. In such case, the selection of a superior filler metal is required for high reliability of brazed ceramic joints. If we inspect previous literatures, we see two major issues that are needed to be minimized in ceramic brazing, such as wetting of the contact

surfaces and the stress development caused by the mismatch in mechanical and thermal properties of two contact materials that depend on the deformation characteristics of the filler used [1–5].

There are various strategies developed to resolve these mentioned issues. First is the use of active metal brazing techniques. Active metal brazing is a simple and cost-effective approach where active elements like Ti or Zr as wetting promoters are used between the contact surfaces for bonding [1, 6]. Therefore, the popular Ag-Cu-Ti filler seems to be more reliable over the Ag-Cu filler due to its good wetting to most of the ceramics [7].

Second is the use of additive elements or reinforcement particles to refine the interfacial layer, redistribute the stress in the matrix, and relax the joint stress. These secondary phases act as a wetting enhancer when used in optimum amounts [8, 9]. It was reported that the use of reinforcements provides outstanding benefits in terms of joint strength and interfacial characteristics [10, 11]. In the

past, the use of nanomaterials has already been suggested as a potential technology for controlling the wetting, refining the grains, IMCs, as well as to tailor the joint microstructure [8–11]. In lead-free soldering, a variety of nanoparticles have found a wide scope in popular Sn-based alloys for tailoring the microstructure containing harmful  $\text{Cu}_6\text{Sn}_5$  and  $\text{Cu}_3\text{Sn}$  IMCs across the Cu-Sn interface [12–14]. Analogous to brazing, nanoparticles have been tried in few studies related to the low-temperature Al-brazing filler and remarkably improved wetting and joint performance are obtained. Al-brazing fillers have been embedded with SiC,  $\text{La}_2\text{O}_3$ , and  $\text{ZrO}_2$  successfully in low-temperature Al-brazing [11]. There are various studies in the past where researchers have used metal or nonmetallic additives to control the brazing performance. More recently, Shin and his coworkers have improved the wetting and brazing property of  $\text{Al}_2\text{O}_3/\text{Cu}$  joints with the addition of Sn in the Ag-Cu-Ti alloy during the brazing process [3]. Halbig and his coworkers used SiC particles in the Ag-Cu-Ti matrix for SiC brazing [15]. Miao et al. used graphite particles to improve the performance of metal-bonded high-speed grinding wheels [16]. Zhao et al. used  $\text{MoS}_2$  particles to enhance tribological properties of cubic boron nitride abrasive composites [17]. In another study, Miao et al. recommended that TiX additives in the Ag-Cu-Ti matrix ( $\text{TiB}_2$ , TiN, and TiC) improve the shear strength of the brazed joints [18]. Most popular nanoreinforcements used regularly to reinforce a metal alloy include  $\text{Al}_2\text{O}_3$ , SiC,  $\text{ZrO}_2$ ,  $\text{SnO}_2$ ,  $\text{CeO}_2$ ,  $\text{La}_2\text{O}_3$ , and  $\text{ZrSiO}_4$  [14, 15, 19–23]. However, in ceramic brazing, limited studies exist on nanocomposite-based brazing fillers [24–26]. Among these nanoreinforcements, rare earth oxide, particularly,  $\text{CeO}_2$ , has been used frequently for low temperature joining of electronic devices as well as in multiple applications such as photonics, energy storage devices, sensing, and power electronics.

In view of these merits, we have chosen  $\text{CeO}_2$  nanoparticles produced via solution combustion method to reinforce the Ag-Cu-Ti matrix and apply for brazing of  $\text{ZrO}_2$  and Ti-6Al-4V plates in the lap-joint configuration. The microstructural, mechanical, and thermal properties of the composite fillers were studied. The effect of various fractions of  $\text{CeO}_2$  ( $x=0, 0.03, 0.05$ , and  $0.1$  wt%) in the Ag-Cu-Ti matrix was studied for microstructure, wetting and brazed joint  $\text{ZrO}_2$ , and Ti-6Al-4V strength.

## 2. Materials and Methods

**2.1. Synthesis of  $\text{CeO}_2$  Powder.** Cerium oxide nanopowder was prepared by using the high-temperature solution combustion method using ceric ammonium nitrate, citric acid, and glycine [27]. All the chemicals were of reagent grade supplied by Sigma Aldrich, USA.

**2.2. Base Materials.** The base materials used for brazing were  $\text{ZrO}_2$  and Ti-6Al-4V (Grade 5, ELI plate) rectangular plates obtained from Acucera, Inc., South Korea, and United Performance, USA, respectively. Both the base materials

were diced by using a diamond saw into slices with a size of  $60.0 \text{ mm} \times 15.0 \text{ mm} \times 2.0 \text{ mm}$  for brazing and shear testing.

**2.3. Synthesis of Composite.** Four different types of composite fillers with different  $\text{CeO}_2$  contents were used in the experiment, as shown in Table 1. The powder mixtures were blended in a planetary mill (Planetary Ball Mill PM 400 Retsch, Germany) at 300 rpm for 24 hours (ball to powder weight ratio = 15:1). After milling, the mixed powder samples were mixed with Nocolok flux (10:1 ratio) and melted at  $1050^\circ\text{C}/30$  minutes in a tube furnace.

**2.4. Brazeability.** The brazeability of the composite fillers was determined from the spreading ratios of filler melted before and after melting (Figure 1).

The solidified composite filler (0.3 g approx.) was mixed with Nocolok flux (10:1 ratio) and placed over the substrate ( $30 \text{ mm} \times 30 \text{ mm} \times 2 \text{ mm}$ ) at  $920^\circ\text{C}$ . After a gap of 30 s, the filler was melted completely over the substrate. The spreading ratio ( $S$ ) was estimated from the difference in the spread ratios before and after experiment [28].

**2.5. Melting Point.** The effect of  $\text{CeO}_2$  nanoparticles on the melting behavior of composite fillers was studied by using differential scanning calorimeter (DSC) apparatus (NETZSCH STA 449 F1). About 6–8 mg of specimens were heated in  $\text{Al}_2\text{O}_3$  pans from 28 to  $1000^\circ\text{C}$  at a heating rate of  $10^\circ\text{C}/\text{minute}$  under the Ar atmosphere to minimize air oxidation.

**2.6. Joint Fabrication.** The composite filler was rolled down to a thickness of 0.25 mm and then applied between  $\text{ZrO}_2$  and Ti-6Al-4V alloy in a lap-joint structure. The whole assembly was brazed at  $980^\circ\text{C}$  for 10 min in a vacuum furnace at  $5 \times 10^{-6}$  Torr, as shown in the lap-joint structure in Figure 2.

**2.7. Microstructure.** The phase evolution and structure were determined by using X-ray diffractometer (XRD) from Bruker's D8 Advance, Germany, at operating parameters of 40 mA and 40 kV and copper target ( $\lambda = 0.154 \text{ nm}$ ). The surface morphology of the developed composite fillers and joint cross section were examined in a field emission scanning electron microscope (FE-SEM, Hitachi, Japan). To observe the distinct features of the interface, the joint cross section was etched by using an aqueous solution of  $\text{FeCl}_3$ ,  $\text{H}_2\text{O}$ , HCl, and  $\text{C}_2\text{H}_5\text{OH}$ . The compositional analyses of the IMCs and phases were done by using the EDS detector attached to the FE-SEM.

**2.8. Filler Microhardness.** Microhardness of the developed composite fillers was measured by using a Vickers' microhardness tester (VMHT-6, Leica). The testing parameters include an applied load of 25 gf for a dwell time of 20 s, respectively. The microhardness was automatically calculated and displayed over the display panel of the machine.

TABLE 1: Composition of various composite fillers used.

Serial no.	Filler matrix	Reinforcement nanoceria ( $x$ in wt.%)	Sample ID
1	Ag-28Cu-2Ti	$x = 0$	Ag-Cu-Ti
2		$x = 0.03$	Ag-Cu-Ti-0.03 CeO <sub>2</sub>
3		$x = 0.05$	Ag-Cu-Ti-0.05 CeO <sub>2</sub>
4		$x = 0.1$	Ag-Cu-Ti-0.1 CeO <sub>2</sub>



FIGURE 1: Schematic diagram for the measurement of brazeability.

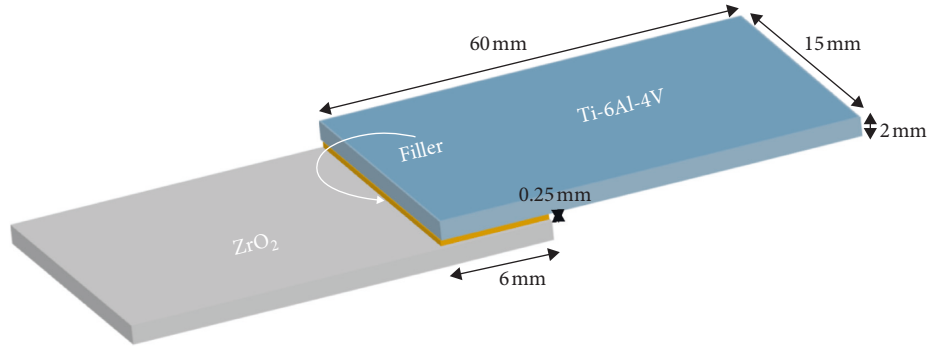


FIGURE 2: Schematic diagram for brazed joint fabrication.

**2.9. Brazing Joint Performance: Shear Test.** The shear strength of the joint was estimated according to the JIS Z 3192 standard [29]. The testing was done by employing a universal testing machine (5 ton UTM, DUT-30000 CM, DK Eng., Korea) at a crosshead speed of 3 mm/minute. The schematic of the set-up used for the shear test is shown in Figure 3.

### 3. Results and Discussion

**3.1. Reinforcement.** Figure 4(a) shows the XRD pattern of the CeO<sub>2</sub> powder (according to ICDD#00-034-0394) obtained after solution combustion synthesis [30]. The peak broadening indicates the nanocrystallinity of the powder with an increased lattice strain. The average crystallite size ( $D$ ) of the powder particles is given by the Scherrer equation [27]:

$$D = \frac{0.9\lambda}{B \cos \theta} \quad (1)$$

In general, the XRD peak broadening is governed by various factors such as the instrumental effects, crystallite size, and lattice strain. Here,  $\lambda$  is the wavelength of X-rays,  $\theta$  is the Bragg angle, and  $B$  is the line broadening at full-width half-maximum intensity calculated from the broadening of a

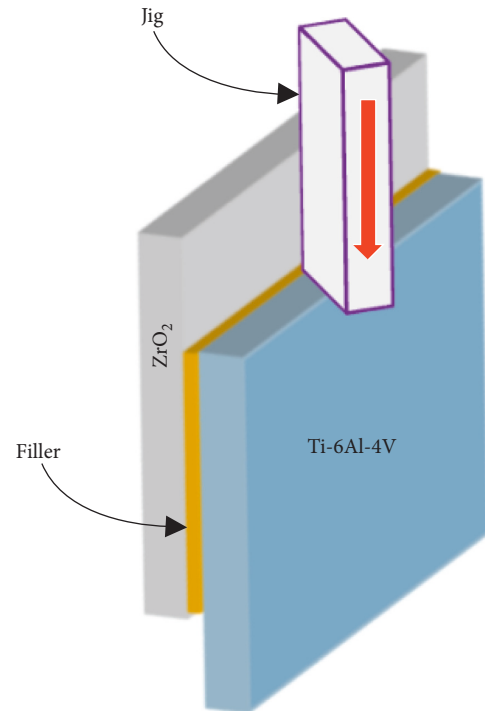


FIGURE 3: Schematic diagram for the shear test.

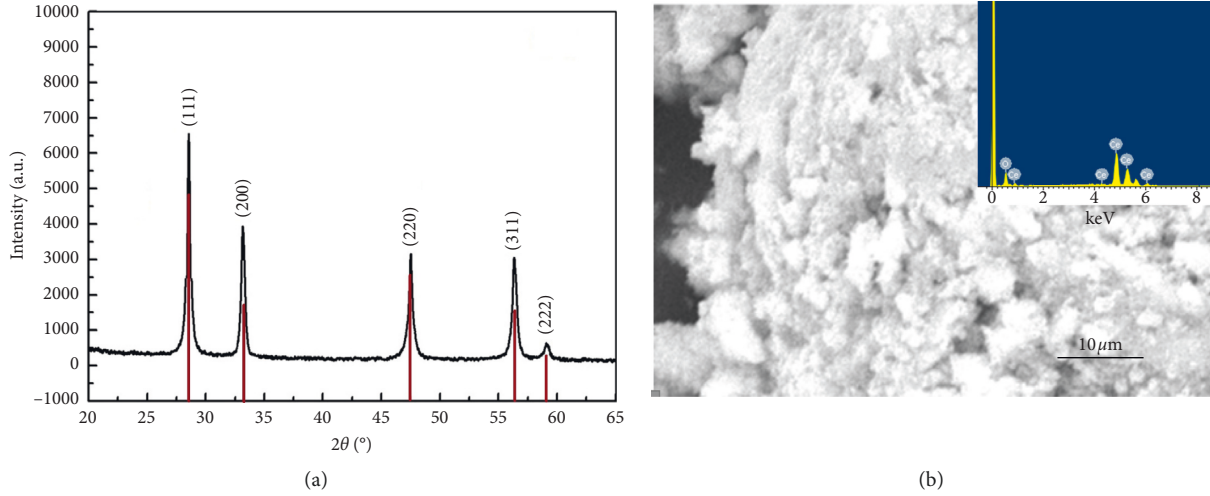


FIGURE 4: (a) XRD pattern (according to ICDD#00-034-0394) and (b) morphology of the ceria nanoparticles. The inset shows the EDS analysis of produced ceria nanopowder.

standard stress-free sample and instrumental broadening contributions, given by

$$B = \sqrt{B_{\text{standard}}^2 - B_{\text{instrumental}}^2} \quad (2)$$

The contribution to lattice strain is given by a modified Scherrer equation:

$$B \cos \theta = \frac{0.9\lambda}{D} + \varepsilon \sin \theta. \quad (3)$$

The crystallite size  $D$  can be calculated from the peaks in the XRD pattern, and the average value of lattice strain was determined from the intercept at  $\cos \theta = 0$  and the slope of  $B \cos \theta$  versus  $\sin \theta$ .

The crystallite size was found to lie in the range of 20–30 nm with the average lattice strain of  $\text{CeO}_2$  powder around 0.39. It is to be noted that as the particle size reduces, the number of surface atoms increases as compared to the bulk. This increase in the surface atoms per unit volume raises the lattice strain which is associated with the structural distortion. This results in high reactivity of the particles at nanoscale level.

The morphology of the  $\text{CeO}_2$  powder particles (Figure 4(b)) is like loose spongy type which is a typical morphology obtained for combustion synthesized powder [27]. This type of structure is already observed in the past by several researchers. The EDS analysis in the inset of Figure 4(b) confirms the composition of the  $\text{CeO}_2$  powder nanopowder.

**3.2. Composite Phase and Microstructure.** Figure 5 shows the XRD pattern of  $\text{Ag-Cu-Ti-xCeO}_2$  composite fillers. The results indicated various peaks in the XRD spectrum. The phases detected were Ag (ICDD# 01-071-3752), Cu (ICDD#00-004-0836),  $\text{Cu}_2\text{Ti}$  (ICDD# 00-020-0371), and  $\text{Cu}_4\text{Ti}$  (ICDD# 00-020-0370) diffraction peaks [30]. The X-ray patterns of other samples were almost similar. There was no indication of the formation of new phases related to  $\text{CeO}_2$  which indicated that there is no reaction of the filler matrix with the reinforcement particles (Figure 5(a)). The  $\text{CeO}_2$  particles were not present in the XRD spectrum which

could be attributed to a very low amount of  $\text{CeO}_2$  nanoparticles to be detected by the XRD analysis.

The different morphology of the composite fillers is shown in Figures 5(b)–5(e). We can see that the addition of  $\text{CeO}_2$  nanoparticles has a great effect on the filler morphology. The corresponding phases were analyzed by the EDS, as shown in Figures 5(b)–5(d) and 5(f). The bright and dark phases are shown by spots 1 and 2, while Cu-Ti IMCs are distributed across the interface (spot 3), as shown in Figure 5(f). The EDS analysis results given in Table 2 also show the probable compositions of the phases of spots 1–3.

After the addition of  $\text{CeO}_2$  nanoparticles, the Ag- and Cu-rich regions were found to be smaller up to the addition of 0.03 wt%  $\text{CeO}_2$ . In other words, there is a refinement in the microstructure of the filler alloy. Generally, the morphology of the composite filler is refined by the addition of nanoparticles into the filler matrix. There are various theories proposed in the past that explain the effect of nanoparticles on composite morphology. According to the absorption theory of surface-active materials [8–11], addition of nanoparticles decreases the surface-free energy of the crystal plane where maximum adsorption of nanoparticle occurs. More precisely, the amount of adsorption of nanoparticles per unit area of  $j$ th plane is given by the following equation:

$$\Gamma^j = -\frac{C}{RT} \left( \frac{d\gamma^j}{dC} \right), \quad (4)$$

where  $RT$  represents the thermal energy/mole,  $C$  is the concentration of nanoparticles, and  $\gamma^j$  represents the surface energy/area of the  $j$ th plane before the adsorption of nanoparticles. After integration of equation (4), we get

$$\gamma_C^j = \gamma_0^j - RT \int_0^C \frac{\Gamma^j}{C} dC, \quad (5)$$

where  $\gamma_C^j$  represents surface energy/area of  $j$ th plane after adsorption of nanoparticles and  $\gamma_0^j$  is the surface energy/area of the  $j$ th plane before adsorption. The resultant surface energy is given from equation (5):



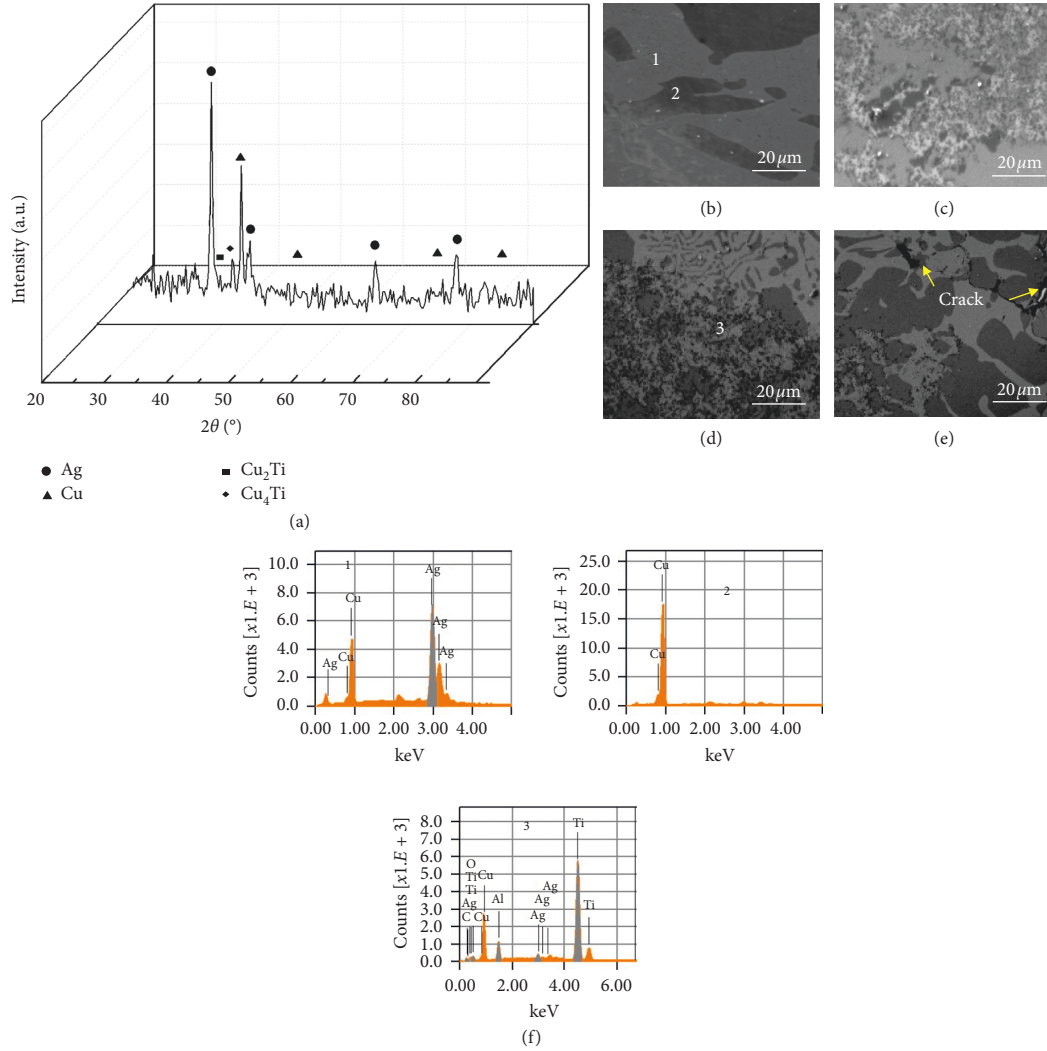


FIGURE 5: (a) XRD pattern of Ag-Cu-Ti- $x\text{CeO}_2$  ( $x=0.1$  wt%) and (b–e) morphology of the Ag-Cu-Ti- $x\text{CeO}_2$  filler,  $x=0, 0.03, 0.05,$  and  $0.1$  wt%. (f) EDS analysis of different phases in (b) and (d).

TABLE 2: EDS data of different phases in Figures 5(b)–5(d).

Serial no.	Sample ID	Cu (at.%)	Ag (at.%)	Ti (at.%)	Phase
1	Point 1	36.41	63.59		Ag-Cu
2	Point 2	100.00	0		Cu
3	Point 3	31.72	1.48	66.8	$\text{Cu}_2\text{Ti}$

$$\sum_j A_j \gamma_k^j = \sum_j \left( \gamma_0^j - RT \int_0^C \frac{\Gamma^j}{C} dC \right) A_k, \quad (6)$$

where  $A_j$  represents the surface area of  $j$ th plane and  $\sum_j A_j \gamma_0^j$  is independent of concentration. Therefore, surface energy will be minimum when  $RT \int_0^C \Gamma^j / C dC$  is maximized [8–13]. Thus, the growth velocity of a particular plane,  $j$ , will be decreased. Since the size of  $\text{CeO}_2$  is around 20–30 nm, the size of the IMCs is of the order of several micrometers. As a result, the nanoparticles can be adsorbed easily to the IMC plane and restrict their growth.

Another theory for the effect of nanoparticles on morphology says that nanoparticles act as nucleating agents, and,

therefore they increase more nucleation sites in the matrix as well as on the IMCs during solidification [8–13]. Therefore, according to the aforementioned theories, the presence of an optimum amount of nanoparticles into the filler matrix will promote the grain and IMC refinement of the filler.

However, for  $x = 0.1$  wt%, the filler microstructure shows the presence of a few cracks (Figure 5(e)). This may be due to the high amount of  $\text{CeO}_2$  nanoparticles getting segregated in due course, and localized cracking was noticed [9–11]. It has been reported by many researchers that high surface-active nanoparticles have a tendency of agglomeration. When the nanoparticle content increases in the matrix ( $x \geq 0.05$  wt%), the interparticle distance among them decreases and they tend to segregate in the matrix. This localized segregation results in buildup of porosity and cracks may form in the joint after solidification [11–13].

**3.3. Brazeability.** Wettability of Ag-Cu-Ti- $x\text{CeO}_2$  filler on the  $\text{ZrO}_2$  and Ti-6Al-4V substrates is shown in Figure 6. It

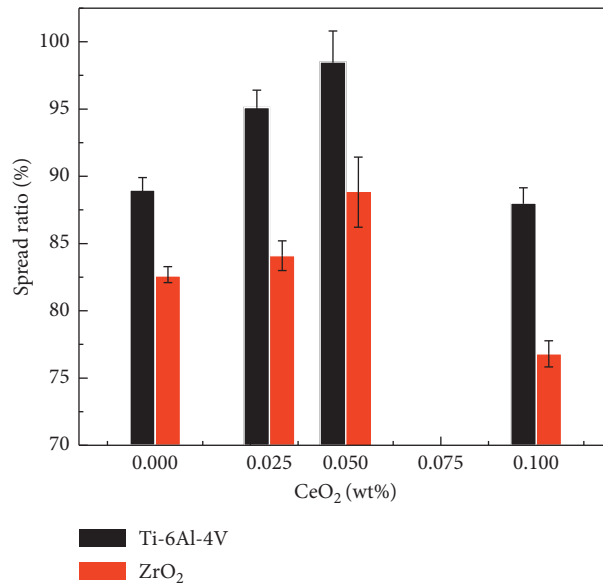


FIGURE 6: Spreading ratio of various Ag-Cu-Ti- $x$ CeO<sub>2</sub> composites on Ti-6Al-4V and ZrO<sub>2</sub> substrates.

was observed that the spreading ratio rises continuously with the increase in CeO<sub>2</sub> fraction in the filler. When the content of CeO<sub>2</sub> was more than 0.05 wt%, the spreading ratio drops considerably and the spreadability of composite filler was decreased. The spreading ratio of the pure Ag-Cu-Ti was approximately 89% on Ti-6Al-4V and 83% on zirconia, which approached to a maximum of 98% on Ti-6Al-4V and 89% on zirconia. The spread ratio though decreased severely with the further addition of CeO<sub>2</sub> nanoparticles reaching up to 87% on Ti-6Al-4V but only 76% on zirconia side. This can be correlated with the presence of high surface energy ceria nanoparticles which depress the surface tension of the filler and enhance the wetting [20]. However, at a high amount of ceria nanoparticles in the matrix, the viscosity of the filler increases and therefore wetting decreases instead of the presence of the active Ti element [20].

It is also noted that, in spite of a higher spreading ratio on Ti-6Al-4V, it decreased up to some extent on zirconia substrates. This is obvious due to the presence of strong covalent bonding in zirconia ceramics compared to the metallic ones in metal. It can be concluded that the addition of an optimum amount of CeO<sub>2</sub> nanoparticles (0.05 wt%) enhances the spreading well on both zirconia as well as Ti-6Al-4V substrates.

**3.4. Melting Point.** Figure 7 represents DSC curves of the produced composite fillers Ag-Cu-Ti- $x$ CeO<sub>2</sub>. Only one sharp melting peak is noticed. The melting point of Ag falls near 961.8°C. The phase diagram of Ag-Cu shows the melting point of Ag-Cu lying near 779°C. Although Ti and CeO<sub>2</sub> components are present, the onset melting point lies around the eutectic melting point 781–778°C. The melting point of Ag-Cu-Ti- $x$ CeO<sub>2</sub> fillers is slightly higher but falls within the normal working limits of brazing. The various onset melting points and peak melting temperature of the composite fillers are shown in Table 3.

The filler alloy ( $x=0$ ) has a peak melting point at 786.5°C which changes to 784.8°C and 783.1°C for composite fillers with  $x=0.03$  CeO<sub>2</sub> and  $x=0.05$  CeO<sub>2</sub>. The difference between the onset melting point (solidus) and peak melting (liquidus), the so-called pasty range, is very narrow (<10°C). A narrow pasty range has been reported to benefit the joining process as it avoids the defects like porosity and/or hot tear that occurs during thermal fluctuations [20, 21]. In other words, the change in the melting point of Ag-Cu-Ti- $x$ CeO<sub>2</sub> composites is not high enough to bring any change in service temperature conditions.

**3.5. Microstructure of the ZrO<sub>2</sub>/Ti-6Al-4V Joint.** Figures 8(a)–8(d) show the SEM image of the ZrO<sub>2</sub>/Ti-6Al-4V interface brazed at 980°C. The interface zone is composed of several black and white patches. The interfacial elements were identified by the EDS analysis (Figure 8(e)). The spot 1 shows a fine layer near the Ti-6Al-4V side. The white and black phases (spots 2 and 3) correspond to the Ag- and Cu-rich phases. The at.% of Cu/Ti ratios were about 1:2 (23.95%: 51.16%) at spot 1a and 1:4 (14.26%: 49.34%) at spot 1b, respectively. This indicates the IMCs are composed of Cu<sub>2</sub>Ti + Cu<sub>4</sub>Ti. Also, Ag (79.37%) and Cu (84.28%) were mainly detected in spot 2 (white color) and 3 (black color).

Ti was prominent near the interface as shown although it existed a little across the interface. A thick layer of Cu<sub>2</sub>Ti is present near the Ti-6Al-4V which is related to the diffusion of Ti from Ti-6Al-4V and Cu from the filler metal to form an excellent bond [4]. The IMC thicknesses of Ag-Cu-Ti filler ( $x=0$  and 0.03) are 18.5 and 22.8  $\mu$ m. The IMC thickness for  $x=0.03$  is higher as compared to  $x=0$ . The reason can be a very small amount which is not sufficient enough to minimize the IMCs considerably in the matrix. The thickness of this layer is different for each condition being minimum (12.4  $\mu$ m) at  $x=0.05$ . Also, the thickness of the interfacial

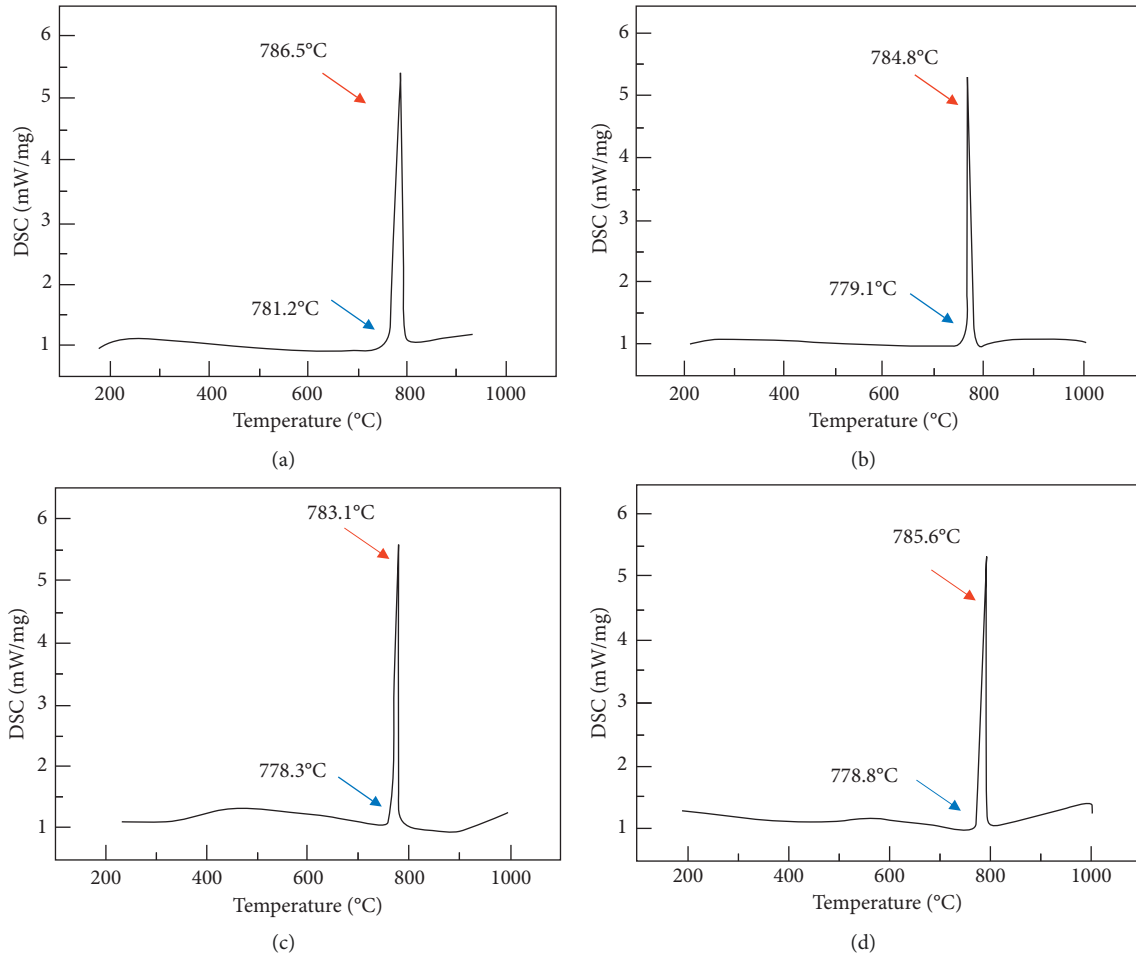


FIGURE 7: Melting point behavior of various Ag-Cu-Ti- $x$ CeO<sub>2</sub> composites: (a)  $x = 0$ ; (b)  $x = 0.03$ ; (c)  $x = 0.05$ ; (d)  $x = 0.1$ .

TABLE 3: Various temperatures obtained from the melting curve of fillers.

Serial no.	Sample ID	$T_{\text{onset m.p.}} (^{\circ}\text{C})$	$T_{\text{peak}} (^{\circ}\text{C})$
1	Ag-Cu-Ti	781.2	786.5
2	Ag-Cu-Ti-0.03 CeO <sub>2</sub>	779.1	784.8
3	Ag-Cu-Ti-0.05 CeO <sub>2</sub>	778.3	783.1
4	Ag-Cu-Ti-0.1 CeO <sub>2</sub>	778.8	785.6

layer is on a little higher side ( $15.4\ \mu\text{m}$ ) for  $x = 0.1$  compared to  $12.4\ \mu\text{m}$  ( $x = 0.05$ ) (Figures 8(c) and 8(d)). This might be due to a higher thickness of Cu<sub>4</sub>Ti along with Cu<sub>2</sub>Ti IMCs at the interface which weakens the bonding. The mechanism of joint formation can be understood by the model presented in Figure 9.

The reaction proceeds in various steps. During brazing, when the temperature is above the solidus of the filler, various elements diffuse to each other across the interface (Figures 9(a) and 9(b)). The filler melts, and then Ti is dissolved into the molten filler and interacts with Cu atoms. Ag occupies the solid solution matrix of the filler. The Cu-Ti IMCs nucleate at the boundaries (Figure 9(c)). The IMC form and grow in due course simultaneously between titanium and ZrO<sub>2</sub>. ZrO<sub>2</sub> is bonded under the influence of Ti

which is absorbed in the surface pores through capillary action at the ZrO<sub>2</sub> surface (Figures 9(c)–9(d)). The CeO<sub>2</sub> nanoparticles are attached to the IMCs and prevent their further growth, as shown by thickness measured from the joint SEM in previous section.

**3.6. Microhardness.** The microhardness values of Ag-Cu-Ti- $x$ CeO<sub>2</sub> composite fillers are given in Table 4. It is seen that the microhardness increases from 115.1 to 126.6 Hv when the CeO<sub>2</sub> content in the filler matrix rises from 0 to 0.05 wt%. This shows a reasonable increase in hardness (11.5%) of the filler matrix. This increase in microhardness value can be ascribed to the fine microstructure containing finer IMCs and Cu- and Ag-rich phases in the Ag-Cu-Ti matrix [31, 32]. The presence of an optimum amount of harder CeO<sub>2</sub> (0.05 wt%) particles in the matrix results in the hindrance of localized plastic deformation of the matrix when CeO<sub>2</sub> particles are present.

A further decrease in hardness (112.5 Hv) is also noticed when 0.1 wt% CeO<sub>2</sub> is added into the filler matrix. Generally, at a high concentration of nanoparticles, the sample hardness should be higher. However, due to high surface energy of CeO<sub>2</sub> nanoparticles, their mixing in the filler powder is not uniform and their incorporation is poor in the solidified

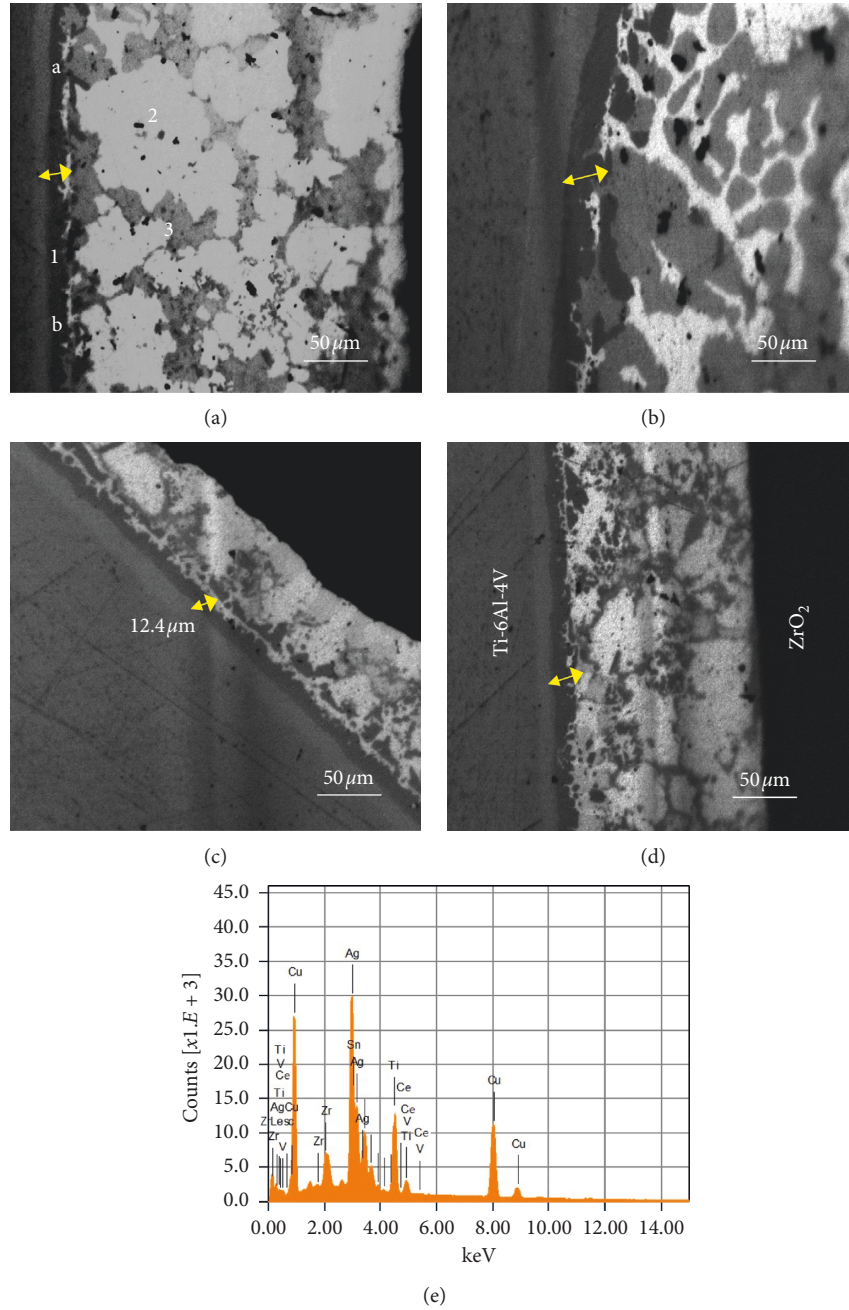


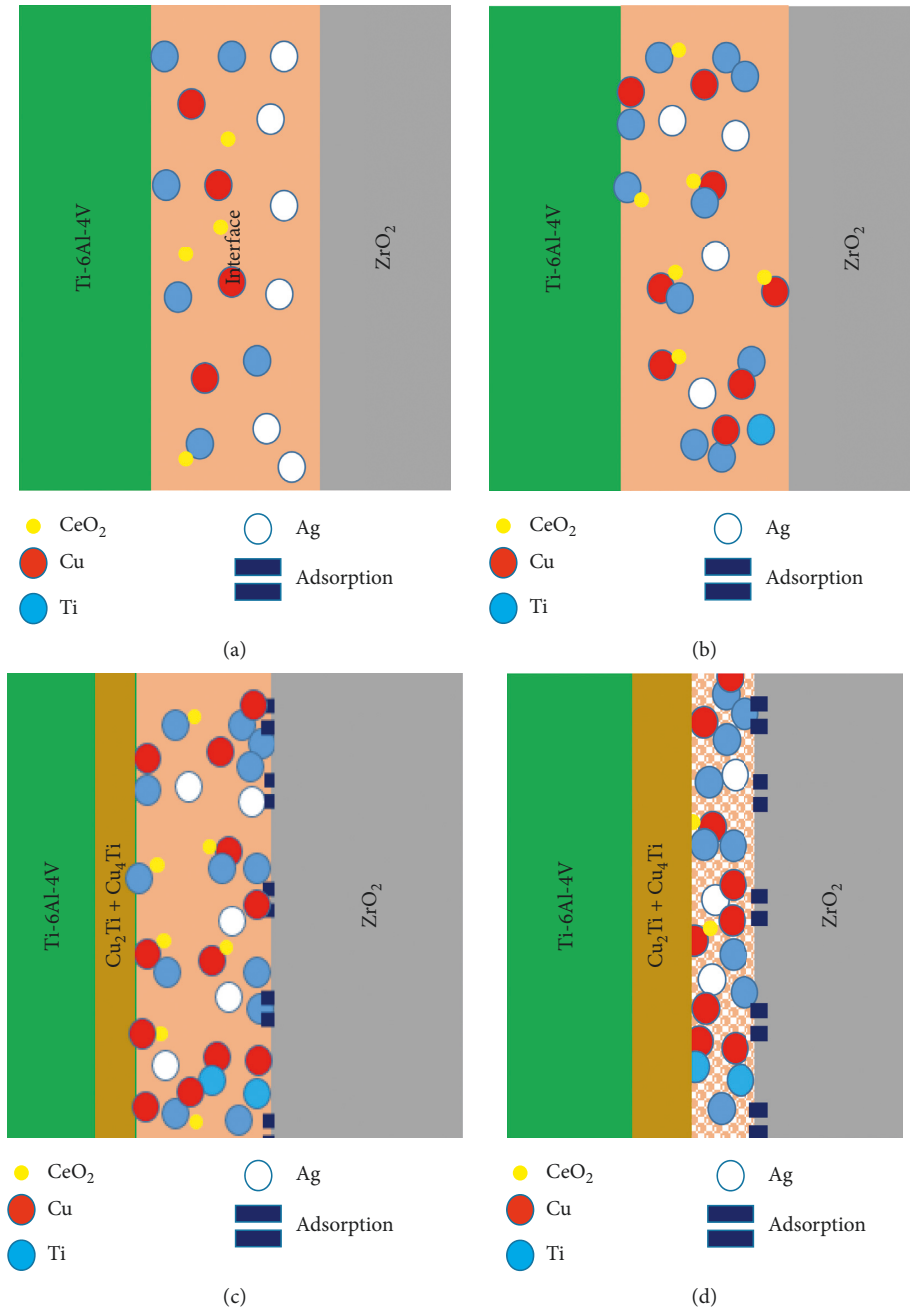
FIGURE 8: The cross-sectional SEM image of the ZrO<sub>2</sub>/Ti-6Al-4V interface brazed using various Ag-Cu-Ti-xCeO<sub>2</sub> composites: (a)  $x=0$ ; (b)  $x=0.03$ ; (c)  $x=0.05$ ; (d)  $x=0.1$ ; (e) EDS analysis of (d).

melt. Therefore, the hardness decrease is associated with two factors: (1) presence of cracks in the sample and (2) poor incorporation of the CeO<sub>2</sub> nanoparticles in the filler matrix at high concentration. This may be due to the increased viscosity and poor wetting of CeO<sub>2</sub> nanoparticles in the melt beyond  $x > 0.05$  wt% [11].

**3.7. Brazed Joint Shear Strength.** The joint shear strength was performed for various composite fillers ( $x=0, 0.03, 0.05$ , and  $0.1$ ). The shear stress-strain diagram is shown in Figure 10. The various shear stress data are shown in Table 5.

It can be seen that the joint shear strength increases with the addition of CeO<sub>2</sub> nanoparticles up to 0.05 wt% in the filler matrix. The sample brazed with filler with  $x=0$  shows a shear strength of  $\sim 19.9$  MPa. The stress increases gradually to 20.4 MPa and 22.8 MPa for the case of  $x=0.03$  and  $0.05$  respectively. The improvement in joint strength at an optimum content of CeO<sub>2</sub> (0.05 wt%) can be attributed to the various factors: (1) presence of harder CeO<sub>2</sub> nanoparticles that obstruct the localized deformation of the matrix, (2) CeO<sub>2</sub> nanoparticles restrict the growth of Cu-Ti IMCs in the filler matrix, and (3) Orowan strengthening due to dislocations form loops around the fine IMCs and CeO<sub>2</sub> particles [8, 11, 13].



FIGURE 9: Schematic for joint formation and bonding of the ZrO<sub>2</sub>/Ti-6Al-4V joint.TABLE 4: Microhardness values of composite fillers as a function of CeO<sub>2</sub> (wt%).

Serial no.	Sample ID	Microhardness (Hv)
1	Ag-Cu-Ti	115.1
2	Ag-Cu-Ti-0.03 CeO <sub>2</sub>	119.4
3	Ag-Cu-Ti-0.05 CeO <sub>2</sub>	126.6
4	Ag-Cu-Ti-0.1 CeO <sub>2</sub>	112.5

The shear strength is decreased to 12.6 MPa for  $x = 0.1$ , as expected. This may be due to the poor spreadability of this sample as already discussed [9–11]. A very high amount of CeO<sub>2</sub> nanoparticles (0.1 wt%) is not desirable in the Ag-Cu-Ti

matrix because it may deteriorate the joint microstructure and strength. This may be due to the high amount of ceria nanoparticles in the melt that decreases the melt fluidity and spreadability [11]. Therefore, it can be concluded from this

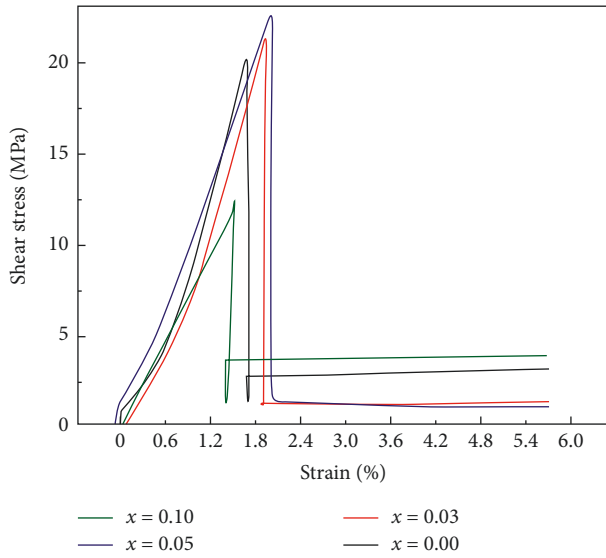


FIGURE 10: Shear stress-strain curves of the various Ag-Cu-Ti- $x$ CeO<sub>2</sub> composites.

TABLE 5: Shear strength data obtained from the shear stress-strain curve.

Serial no.	Sample ID	UTS (MPa)
1	Ag-Cu-Ti	19.9
2	Ag-Cu-Ti-0.03 CeO <sub>2</sub>	20.4
3	Ag-Cu-Ti-0.05 CeO <sub>2</sub>	22.8
4	Ag-Cu-Ti-0.1 CeO <sub>2</sub>	12.6

work that, for an optimum brazing performance of the ZrO<sub>2</sub>/Ti-6Al-4V joint, the desired amount of CeO<sub>2</sub> nanoparticles should not exceed ~0.05 wt% in the Ag-Cu-Ti filler matrix.

#### 4. Conclusions

- (1) The cerium oxide nanoparticles were successfully produced using the solution combustion method. The particle size of the ceria nanoparticles was under 20–30 nm, and lattice strain was around 0.39.
- (2) The Ag-Cu-Ti filler microstructure was composed of Cu-rich and Ag-rich phases and Cu-Ti IMCs. It was found that, with an addition of ceria in the filler matrix (up to 0.05 wt%), the various phases were refined considerably.
- (3) The addition of CeO<sub>2</sub> nanoparticles in the filler matrix improved the wettability of filler on both ZrO<sub>2</sub> and Ti-6Al-4V substrates up to  $x=0.05$  and then decreased dramatically at  $x=0.1$  due to increasing melt viscosity.
- (4) The melting point study shows a depression in the melting point of composite fillers around 3°C when reinforced with 0.05 wt% CeO<sub>2</sub>.
- (5) With the increase in the CeO<sub>2</sub> content, the thickness of the reactive layer (Cu<sub>2</sub>Ti + Cu<sub>4</sub>Ti) between the interface and base materials was reduced

significantly up to the optimum ceria fraction 0.05 wt % in the filler matrix.

- (6) The microhardness of the filler matrix shows an 11.1% increase over the filler matrix when embedded with 0.05 wt% ceria nanoparticles.
- (7) The joint shear test showed that maximum brazed strength was obtained for  $x=0.05$ ; however, it decreased further due to the poor brazeability of filler at  $x=0.1$ .

#### Data Availability

The data used to support the findings of this study are available from the corresponding author upon request.

#### Conflicts of Interest

The authors declare that there are no conflicts of interest regarding the publication of this work.

#### Acknowledgments

This research was supported by Basic Science Research Program through the National Research Foundation of Korea (NRF) funded by the Ministry of Education (NRF-2018R1D1A1B07044481 to B.A. and NRF-2018R1D1A1B07044706 to A.S.).

#### References

- [1] R. M. do Nascimento, A. E. Martinelli, and A. J. A. Buschinelli, "Review article: recent advances in metal-ceramic brazing," *Cerâmica*, vol. 49, no. 312, pp. 178–198, 2003.
- [2] M. B. Uday, M. N. Ahmad Fauzi, M. N. Alias, and S. Rajoo, "Current issues and problems in the joining of ceramic to metal," in *Joining Technologies*, M. Ishak, Ed., InTech Publications, Rijeka, Croatia, 2016.
- [3] J. Shin, A. Sharma, D.-H. Jung, and J. P. Jung, "Effect of Sn content on filler and bonding characteristics of active metal brazed Cu/Al<sub>2</sub>O<sub>3</sub> joint," *Korean Journal of Metals and Materials*, vol. 56, no. 5, pp. 366–374, 2018.
- [4] A. Sharma, S. H. Kee, F. Jung, Y. Heo, and J. P. Jung, "Compressive strength evaluation in brazed ZrO<sub>2</sub>/Ti-6Al-4V joints using finite element analysis," *Journal of Materials Engineering and Performance*, vol. 25, no. 5, pp. 1722–1728, 2016.
- [5] V. Srinivas, A. K. Singh, V. Gopala Krishna, and G. Madhusudhan Reddy, "Vacuum brazing of dissimilar tubular component of AA2219 and AISI 304 by a low melting Al-18Ag-20Cu-5Si-0.2Zn braze alloy," *Journal of Materials Processing Technology*, vol. 252, pp. 1–12, 2018.
- [6] W. D. Kingery, H. K. Bowen, and D. R. Uhlmann, *Introduction to Ceramics*, Wiley-Interscience, Hoboken, NJ, USA, 2nd edition, 1976.
- [7] M. M. Schwartz, *Brazing*, ASM International, Cleveland, OH, USA, 2nd edition, 2003.
- [8] A. Sharma, M.-H. Roh, D.-H. Jung, and J.-P. Jung, "Effect of ZrO<sub>2</sub> nanoparticles on the microstructure of Al-Si-Cu filler for low-temperature Al brazing applications," *Metallurgical and Materials Transactions A*, vol. 47, no. 1, pp. 510–521, 2016.
- [9] A. Sharma, D. U. Lim, and J. P. Jung, "Microstructure and brazeability of SiC nanoparticles reinforced Al-9Si-20Cu

- produced by induction melting,” *Materials Science and Technology*, vol. 32, no. 8, pp. 773–779, 2016.
- [10] A. Sharma, M. H. Roh, and J. P. Jung, “Effect of  $\text{La}_2\text{O}_3$  nanoparticles on the brazability, microstructure, and mechanical properties of Al-11Si-20Cu alloy,” *Journal of Materials Engineering and Performance*, vol. 25, no. 8, pp. 3538–3545, 2016.
  - [11] A. Sharma, D. E. Xu, and J. P. Jung, “Effect of different nanoparticles on microstructure, wetting and joint strength of Al-12Si-20Cu braze filler,” *Materials Research Express*, vol. 6, no. 5, Article ID 056526, 2019.
  - [12] J. Shen and Y. C. Chan, “Research advances in nano-composite solders,” *Microelectronics Reliability*, vol. 49, no. 3, pp. 223–234, 2009.
  - [13] A. Sharma, B. G. Baek, and J. P. Jung, “Influence of  $\text{La}_2\text{O}_3$  nanoparticle additions on microstructure, wetting, and tensile characteristics of Sn-Ag-Cu alloy,” *Materials & Design*, vol. 87, pp. 370–379, 2015.
  - [14] A. Sharma, H. Yu, I. S. Cho, H. Seo, and B. Ahn, “ $\text{ZrO}_2$  nanoparticle embedded low silver lead free solder alloy for modern electronic devices,” *Electronic Materials Letters*, vol. 15, no. 1, pp. 27–35, 2019.
  - [15] M. C. Halbig, B. P. Coddington, R. Asthana, and M. Singh, “Characterization of silicon carbide joints fabricated using SiC particulate-reinforced Ag-Cu-Ti alloys,” *Ceramics International*, vol. 39, no. 4, pp. 4151–4162, 2013.
  - [16] Q. Miao, W. Ding, D. Fu, Z. Chen, and Y. Fu, “Influence of graphite addition on bonding properties of abrasive layer of metal-bonded CBN wheel,” *The International Journal of Advanced Manufacturing Technology*, vol. 93, no. 5–8, pp. 2675–2684, 2017.
  - [17] B. Zhao, W. Ding, W. Kuang, and Y. Fu, “Microstructure and tribological property of self-lubrication CBN abrasive composites containing molybdenum disulfide,” *Industrial Lubrication and Tribology*, vol. 71, no. 5, pp. 712–717, 2019.
  - [18] Q. Miao, W. Ding, Y. Zhu, Z. Chen, and Y. Fu, “Brazing of CBN grains with Ag-Cu-Ti/TiX composite filler—the effect of TiX particles on microstructure and strength of bonding layer,” *Materials & Design*, vol. 98, pp. 243–253, 2016.
  - [19] J. Yang, H. Y. Fang, and X. Wan, “Effects of  $\text{Al}_2\text{O}_3$  particulate contained composite filler materials on the strength of alumina joints,” *Journal of Materials Science & Technology*, vol. 18, no. 4, pp. 289–290, 2002.
  - [20] A. Sharma, A. K. Srivastava, K. Lee, and B. Ahn, “Impact of non-reactive ceria nanoparticles on the wettability and reaction kinetics between lead-free Sn-58Bi and Cu pad,” *Metals and Materials International*, vol. 25, no. 4, pp. 1027–1038, 2019.
  - [21] A. Sharma, A. K. Srivastava, and B. Ahn, “Microstructure, mechanical properties, and drop reliability of  $\text{CeO}_2$  reinforced Sn-9Zn composite for low temperature soldering,” *Materials Research Express*, vol. 6, no. 5, Article ID 056520, 2019.
  - [22] R. Sun, Y. Sui, J. Qi et al., “Influence of  $\text{SnO}_2$  nanoparticles addition on microstructure, thermal analysis, and interfacial IMC growth of Sn1.0Ag0.7Cu solder,” *Journal of Electronic Materials*, vol. 46, no. 7, pp. 4197–4205, 2017.
  - [23] S. Bhattacharya, A. Sharma, S. Das, and K. Das, “Synthesis and properties of pulse electrodeposited lead-free tin-based Sn/ $\text{ZrSiO}_4$  nanocomposite coatings,” *Metallurgical and Materials Transactions A*, vol. 47, no. 3, pp. 1292–1312, 2016.
  - [24] F. Moszner, C. Cancellieri, C. Becker, M. Chiodi, J. Janczak-Rusch, and L. P. H. Jeurgens, “Nano-structured Cu/W brazing fillers for advanced joining applications,” *Journal of Materials Science and Engineering B*, vol. 6, no. 5, pp. 226–230, 2016.
  - [25] H. Bian, Q. Zhang, Y. Song, D. Liu, J. Liu, and X. Song, “Microstructure and mechanical properties of a  $\text{SiO}_2$  ceramic and  $\text{TC}_4$  alloy joint brazed with a nanocomposite filler,” *Journal of Materials Engineering and Performance*, vol. 28, no. 7, pp. 4427–4433, 2019.
  - [26] D. Busbaher, W. Liu, and D. P. Sekulic, “Mechanical properties of nanoparticles reinforced Mo-Ni braze for a dispenser cathode application,” in *Proceedings of the 14th International Vacuum Electronics Conference (IVEC)*, pp. 1–2, IEEE, Monterey, CA, USA, April 2013.
  - [27] A. Sharma, “Effect of synthesis routes on microstructure of nanocrystalline cerium oxide powder,” *Materials Sciences and Applications*, vol. 4, no. 9, pp. 504–508, 2013.
  - [28] A. Sharma, H.-R. Sohn, and J. P. Jung, “Effect of graphene nanoplatelets on wetting, microstructure, and tensile characteristics of Sn-3.0Ag-0.5Cu (SAC) alloy,” *Metallurgical and Materials Transactions A*, vol. 47, no. 1, pp. 494–503, 2016.
  - [29] JIS Z 3192: 1999, *Methods of Tensile and Shear Tests for Brazed Joint*, Japanese Standards Association, Tokyo, Japan, 1999.
  - [30] *Powder Diffraction File, International Center for Diffraction Data (ICDD)*, Newtown Square, PA 19073-3273, USA, <http://www.icdd.com/>.
  - [31] Y. M. He, J. Zhang, C. F. Liu, and Y. Sun, “Microstructure and mechanical properties of  $\text{Si}_3\text{N}_4/\text{Si}_3\text{N}_4$  joint brazed with Ag-Cu-Ti + SiCp composite filler,” *Materials Science and Engineering: A*, vol. 527, no. 12, pp. 2819–2825, 2010.
  - [32] Q. Miao, W. Ding, Y. Zhu, Z. Chen, J. Xu, and C. Yang, “Joining interface and compressive strength of brazed cubic boron nitride grains with Ag-Cu-Ti/TiX composite fillers,” *Ceramics International*, vol. 42, no. 12, pp. 13723–13737, 2016.



